Aerodynamic performance analysis of an isolated UHBR engine using a far-field exergy balance method

Ilias Petropoulos, Fulvio Sartor

Association Aéronautique et Astronautique de France

57th 3AF International Conference on Applied Aerodynamics
29 – 31 March 2023, Bordeaux – France

AERO2023-20

Aerodynamic performance analysis of an isolated UHBR engine using a far-field exergy balance method

Ilias Petropoulos[(1)] and Fulvio Sartor[(2)]

[(1)]*ONERA, 8 rue des Vertugadins, 92190 Meudon, France, ilias.petropoulos@onera.fr*
[(2)]*ONERA, 8 rue des Vertugadins, 92190 Meudon, France, fulvio.sartor@onera.fr*

ABSTRACT

This paper presents the aerodynamic performance study of an isolated ultra-high bypass ratio turbofan engine. The performance assessment methodology relies on an exergy balance, computed using the ONERA FFX software on the basis of RANS CFD solutions. The study first investigates aspects associated with the computational strategy used to simulate engines of this type. This concerns in particular a grid convergence study and a comparison of different types of modelisation methods for the fan and OGV, in terms of the exergy balance. At a second step, an exergy-balance-based analysis of the engine is carried out at different operating conditions. This analysis allows the evaluation of the system's overall performance, while at the same time providing a phenomenological decomposition of mechanical/thermocompressible exergy outflows and the characterization of exergy losses due to irreversible effects.

1. INTRODUCTION

Ultra-high bypass ratio (UHBR) engines constitute one of the main short- to mid-term promising technologies aiming at reducing the specific fuel consumption of civil transport aircraft. Higher bypass ratios in turbofan engines are reached by increasing the diameter of the fan/OGV and engine nacelle. In order to compensate for the overall weight increase due to this larger diameter, UHBR engines feature significantly shorter intake and nozzle lengths in comparison to previous engine generations. As a result, the inlet flow distortion under particular conditions (e.g. crosswind or high angle of attack) can become significant and lead to inlet lip separation that may be ingested by the fan. Specific compromises must therefore be pursued between the inlet length/shape and attributes such as weight, proneness to flow separation, cruise aerodynamic performance and propulsive efficiency (cf. [11] for example). At the same time however, such features can make these configurations challenging for common numerical simulation methods used in the design process of longer-intake engines.

This challenge for numerical methods was a main research subject of the Clean Sky 2 ASPIRE project, on the aerodynamics and acoustics of UHBR turbofan engines. The project was part of the large passenger aircraft platform, and was carried out in a collaboration of ONERA with Airbus, DLR and NLR. In order to address the subject of design methods for such types of configurations, a generic research UHBR engine was designed within the project, in collaboration between its partners. At a second step, this engine model was used as a basis for the comparison of numerical methodologies of varying levels of fidelity. These were compared in terms of standard industrial design performance evaluation methods and ease of implementation [7]. Other computational aspects and code-to-code comparisons on this configuration are discussed in [10].

However, in order to achieve finer efficiency gains on such engine types, it is important that numerical simulation tools are complemented by more advanced methods for the analysis of aerodynamic performance. This is essential at the level of an industrial cycle, where the flow and geometrical complexity require that designers analyse an increasing quantity of numerical simulation data. Industrializable methods are thus expected to be capable of decomposing and quantifying the influence of different flow features on the engine performance, both at an isolated component and at an integrated level on the aircraft. The present work concerns the performance analysis of a generic UHBR engine using an assessment methodology based on an exergy balance [1, 2, 5]. The study is

part of ONERA activities within the ADEC project on advanced engine and aircraft configurations, in the frame of the Clean Sky 2 large passenger aircraft demonstration platform.

In particular, this analysis was carried out by a far-field exergy balance method, on the basis of CFD computations of the UHBR turbofan engine investigated in the ASPIRE project. The aerodynamic performance analysis is composed of the following parts. The first is a grid convergence study on a series of three different grid levels, followed by a study of the influence of the fan/OGV modelling strategy (actuator disks or body-force source terms) on the exergy balance. Finally, the exergy-based analysis of the engine performance is carried out at different operating points corresponding to the aerodynamic design point (cruise) and to low-speed conditions.

2. DESCRIPTION OF THE ENGINE CONFIGURATION

The test case is the research UHBR turbofan engine of the Clean Sky 2 ASPIRE project, henceforth referred to as the "ASPIRE" engine. It corresponds to a model isolated double-stream configuration representative of UHBR turbofan engines, with a bypass ratio around 16. Simplified nacelle, intake and nozzle shapes were designed by Airbus, whereas the fan and OGV blades (composed of 16 and 36 blades respectively) were designed by DLR. Finally, the nacelle features an inlet with a very small length-to-diameter ratio ($\approx$ 0.25-0.35) and a droop angle. A view of the geometry is shown in Fig. 1.

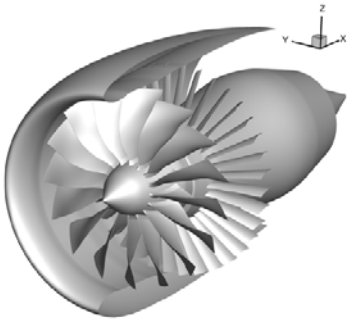

Figure 1: View of the ASPIRE engine geometry.

The main operating conditions investigated were the Aerodynamic Design Point (ADP) and Low-Speed (LS), summarized in Table 1. Investigations at LS conditions were carried out at different angles of attack to analyse the inlet distortion. The Reynolds number corresponds to flight conditions (in the order of 6 million per meter).

Computations of this test case were carried out by the ASPIRE project partners aiming at assessing the capability of different numerical strategies and models to accurately simulate the flow in a design cycle [10]. ONERA

	Altitude [ft]	Mach [-]	α [°]
ADP	35,000	0.8	3
LS	0	0.3	15-35

Table 1: Main operating points for the isolated engine.

studies in this framework were carried out using simplified fan/OGV models (inlet/outlet boundary conditions, actuator disks, body-force source terms), complemented by higher-fidelity computations including the blade geometry (either in a steady framework resolving the flow around the blades in a rotating frame of reference or in a time-accurate framework including the flow unsteadiness) [7]. Additional studies dedicated to the active flow control of intake separation under significant distortion were investigated in [13].

3. COMPUTATIONAL STRATEGY

The test cases analysed in the present work correspond to the actuator-disk and body-force CFD computations discussed in the previous section. The use of such models is particularly appropriate for design studies, in the scope of which time-accurate simulations are too expensive. Actuator disk (AD) computations were carried out using two different models. The first corresponds to a simple uniform pressure jump across the AD interface (AD-UP, applied to the fan only), whereas the second is a higher-fidelity model based on an abacus of blade data generated from isolated fan/OGV RANS computations (AD-AB). Body-force (BF) computations were carried out with source terms based on the modified Hall model [9], generated on the basis of blade geometry characteristics. This means that the fan and OGV blades are not resolved in any of the investigated cases, but each of the modelization types is used to model their effect on the mean flow (cf. Fig. 2).

The test case geometry includes the complete 360° engine, discretized by a series of multiblock structured grids of three refinement levels. The grids are not identical between the actuator disk and body-force cases, but of a similar refinement at each grid level. The coarse, medium and fine grid levels are composed of around 4.8, 28.9 and 195.6 million points respectively. The coarse grid corresponds to an under-refined discretisation oriented towards preliminary investigations, the medium corresponds to a reasonable refinement level for design studies ($y^+ \approx 1$ and approximately 60 points in the boundary layer), whereas the fine one was generated with the view of providing a reference solution to assess grid convergence.

The RANS computations were carried out with the elsA solver (property of ONERA-Airbus-Safran) [8]. This software solves the compressible Navier-Stokes equations using a finite-volume formulation in structured,

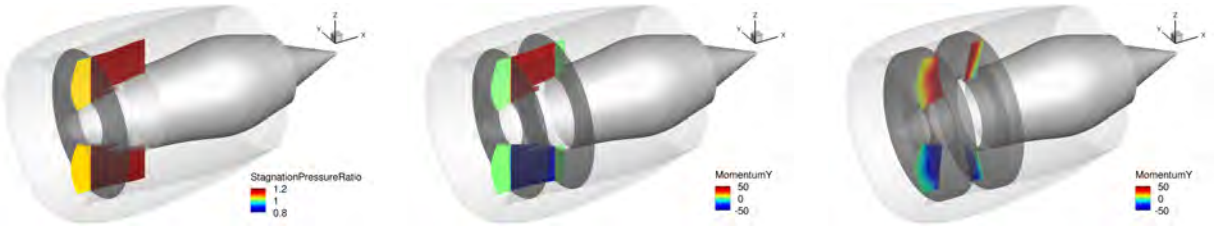

Figure 2: Illustration of the actuator disk and body-force models (left: AD-UP, middle: AD-AB, right: BF). The darker shading highlights the region of application of the corresponding model.

unstructured or hybrid structured/unstructured grids. The solutions investigated in the present study were computed with the reference structured solver, using the $k-\omega$ Wilcox turbulence model. The space discretization is based on the Roe scheme using a second-order interpolation of the primitive variables and the min-mod limiter.

In terms of boundary conditions, walls are considered adiabatic, farfield boundary conditions are applied on the external boundaries of the computational domain, and an inflow condition is applied at the primary stream exhaust. Last, a valve-law boundary condition with radial equilibrium is applied on the primary stream inlet, allowing to reach the target massflow rate by permitting a fluctuation of the pressure field.

4. FAR-FIELD EXERGY BALANCE FORMULATION

ONERA has been working on methods for aerodynamic performance assessment for several years, in particular regarding the computation and phenomenological decomposition of aerodynamic drag [3]. More recently, in the family of far-field methods, a different framework was developed based on the concept of exergy [1, 2, 5]. Exergy expresses the maximum work that is theoretically recoverable from a system, with respect to the thermodynamic conditions of a reference reservoir. Considering a perfect gas hypothesis and neglecting gravitational potential energy, specific exergy can be defined as:

$$\chi = \delta e + p_\infty \delta\left(\frac{1}{\rho}\right) - T_\infty \delta s + \frac{1}{2}\left(\mathbf{V}-\mathbf{V}_\infty\right)^2 \qquad (1)$$

where e is specific internal energy, ρ is density, p is pressure, T is temperature, s is specific entropy, $\mathbf{V}$ is the velocity vector, and finally $\delta(\bullet) = (\bullet) - (\bullet)_\infty$ is the perturbation of a quantity with respect to the reference state (denoted by the subscript $_\infty$). Note that the above definition holds for a reference state that is not at rest (cf. [6]). In the case of a fluid in steady motion, specific flow exergy can be expressed as:

$$\chi_f = \delta h - T_\infty \delta s + \frac{1}{2}\left(\mathbf{V}-\mathbf{V}_\infty\right)^2 \qquad (2)$$

where h is specific enthalpy. The present paper only considers the analysis of steady-state solutions, meaning that the analysis concerns time-averaged changes in exergy.

Only a brief presentation of the formulation is presented in the present section. For details on its derivation and theoretical analyses, readers are referred to the aforementioned references. Under the above considerations, an exergy balance can be formulated in a control volume (c.v.) V enclosed by an outer surface S_o, containing a configuration the surface of which is denoted S_b. In the present case, boundaries of integration domains are considered adiabatic and the solutions are computed in an inertial frame of reference. The exergy balance in this case can be simplified to the following compact form:

$$\boxed{\dot{\mathrm{X}}_{tf} = W\dot{\Gamma} + \dot{\mathrm{X}}_m + \dot{\mathrm{X}}_{th} + \dot{\mathrm{A}}_{tot}} \qquad (3)$$

with the analytical expression of each term described in the following.

$$\dot{\mathrm{X}}_{tf} = -\int_{S_p} \rho\left(\delta h + \frac{1}{2}\left(\mathbf{V}^2 - \mathbf{V}_\infty^2\right) - T_\infty \delta s\right)\mathbf{V}\cdot\mathbf{n}\,dS \qquad (4)$$

represents the inflow or outflow of flow exergy across throughflow surfaces such as permeable boundary conditions, actuator disk interfaces or body-force term regions (corresponding to the surface S_p). Note that this is equivalent to the original definition [1, 2] (cf. [6] for further details). It corresponds to a definition of exergy with respect to a dead state which is at rest in a reference frame attached to the aircraft, and a subtraction of the free-stream kinetic energy.

$$W\dot{\Gamma} = \int_{S_o} \rho u V_\infty\left(\mathbf{V}\cdot\mathbf{n}\right) + \left(p - p_\infty\right)\left(\mathbf{V}_\infty\cdot\mathbf{n}\right)dS \qquad (5)$$

represents the rate of mechanical exergy consumption associated with the configuration's off-equilibrium overall streamwise force balance. The term $\dot{\mathrm{X}}_m$ represents the mechanical exergy outflow, and can be decomposed as follows:

$$\begin{aligned}
\dot{\mathrm{X}}_m &= \dot{E}_u + \dot{E}_{vw} + \dot{E}_p \\
\dot{E}_u &= \int_{S_o} \frac{1}{2}\rho u^2\,\mathbf{V}\cdot\mathbf{n}\,dS \\
\dot{E}_{vw} &= \int_{S_o} \frac{1}{2}\rho\left(v^2+w^2\right)\mathbf{V}\cdot\mathbf{n}\,dS \\
\dot{E}_p &= \int_{S_o} \left(p-p_\infty\right)\left(\mathbf{V}-\mathbf{V}_\infty\right)\cdot\mathbf{n}\,dS
\end{aligned} \qquad (6)$$

into the streamwise perturbation kinetic energy outflow from the c.v. ($\dot{E}_u$), the corresponding transversal perturbation kinetic energy outflow from the c.v. ($\dot{E}_{vw}$) and the rate of pressure work on the c.v. outer boundary associated with these perturbations ($\dot{E}_p$). Note that since exergy of mechanical nature is theoretically fully recoverable, it is equivalent to mechanical energy (i.e. $\dot{\mathrm{X}}_m = \dot{E}_m$).

$$\dot{\mathrm{X}}_{th} = \int_{S_o} \rho \delta e \, \mathbf{V} \cdot \mathbf{n} \, dS + \int_{S_o} p_\infty \left(1 - \frac{\rho}{\rho_\infty}\right) \mathbf{V} \cdot \mathbf{n} \, dS - \int_{S_o} T_\infty \rho \delta s \, \mathbf{V} \cdot \mathbf{n} \, dS \tag{7}$$

represents the outflow of thermocompressible exergy from the c.v. The last term in Eq. (3) represents the total rate of anergy generation, or equivalently exergy loss, due to irreversible processes:

$$\begin{aligned} \dot{\mathrm{A}}_{tot} &= \dot{\mathrm{A}}_\phi + \dot{\mathrm{A}}_{\nabla T} + \dot{\mathrm{A}}_w \\ \dot{\mathrm{A}}_\phi &= \int_V \frac{T_\infty}{T} \phi_{\mathrm{eff}} \, dV \\ \dot{\mathrm{A}}_{\nabla T} &= \int_V \frac{T_\infty}{T^2} k_{\mathrm{eff}} (\nabla T)^2 \, dV \\ \dot{\mathrm{A}}_w &= \int_{S_w} T_\infty [\![\frac{1}{T} \mathbf{q}_{\mathrm{eff}} + \rho \delta s \, \mathbf{V}]\!] \cdot \mathbf{n} \, dS \end{aligned} \tag{8}$$

It can be decomposed into three components $\dot{\mathrm{A}}_\phi$, $\dot{\mathrm{A}}_{\nabla T}$, $\dot{\mathrm{A}}_w$ which respectively represent the anergy generation associated with viscous effects, thermal diffusion and shockwaves.

In the above, $[\![\bullet]\!]$ denotes the jump of a quantity across the corresponding surface, $\overline{\overline{\tau}}_{\mathrm{eff}}$ is the effective viscous stress tensor, $\mathbf{q}_{\mathrm{eff}} = -k_{\mathrm{eff}} \nabla T$ is the effective heat flux by conduction, $\phi_{\mathrm{eff}} = \left(\overline{\overline{\tau}}_{\mathrm{eff}} \cdot \nabla\right) \cdot \mathbf{V}$ is the effective dissipation rate per unit volume and u, v, w are the velocity perturbation components.

In the general case, the exergy balance equation is not satisfied at the discrete level, due to errors associated with the discretization in the case of numerical solutions. Different indicators have been formulated, aiming at quantifying and decomposing this error. Two of these are the discrete error in the energy conservation and the entropy equation, noted $\dot{E}^*$ and $\dot{\mathrm{A}}^*$ respectively, whereas the exergy balance residual is noted $\dot{\mathrm{X}}^*$ [5]. In addition, a quantification of an important part of purely numerical effects is possible by the spurious anergy term $\dot{\mathrm{A}}_{sp}$ ($\dot{\mathrm{A}}_{sp} \leq \dot{\mathrm{A}}^*$) [12].

In practice, the control volume extends far in the upstream and lateral directions, but is limited by a downstream transverse plane (its position noted as x_{tp}), which in the current case is measured with respect to the position of the trailing edge of the engine nacelle. Integration regions (i.e. volumes or surfaces) are defined by appropriate physical sensors, often with the addition of a few layers to include eventual numerical oscillations [1, 5]. The resulting exergy balance terms are commonly presented in the form of non-dimensional coefficients $C(\bullet) = (\bullet)/(0.5\rho_\infty V_\infty^3 S_{ref})$, with their values in power counts (10^{-4}).

The above formulation is integrated in the FFX (far-field exergy) post-processing software of ONERA dedicated to the analysis of CFD solutions. The code has a modular architecture with an interface in Python, allowing significant flexibility in scripting and coupling, whereas internal operations are handled in a C++ level allowing to combine the flexibility with computational performance. A large part of operations is closely coupled with the Cassiopée pre-/post-processing library developed at ONERA [4]. The code can accurately analyse finite-volume CFD solutions on structured, unstructured or overset (Chimera) grids, with the solution computed at cell centers or at vertices. It can also analyse several industrial models such as actuator disks, heat exchanger models, body-force source terms or complex boundary conditions (e.g. mixing plane boundaries between turbomachinery rows).

5. AERODYNAMIC PERFORMANCE ANALYSIS

5.1 Grid convergence study

At a first step, a grid convergence study has been performed for the body-force computations at the ADP operating point. The resulting exergy balance breakdown is shown in Fig. 3. More detailed results on the exergy balance terms are shown in Table 2.

These results highlight that the most significant variations are observed in the grid convergence of the $C_{W\dot{\mathrm{I}}}$ and the viscous/thermal anergy terms. As shown in Fig. 3, the thermocompressible exergy outflow (mainly associated with the primary stream jet) is shown to be approximately 2.65 times more important than mechanical exergy outflow at the ADP operating point, with the most significant mechanical component being associated with streamwise

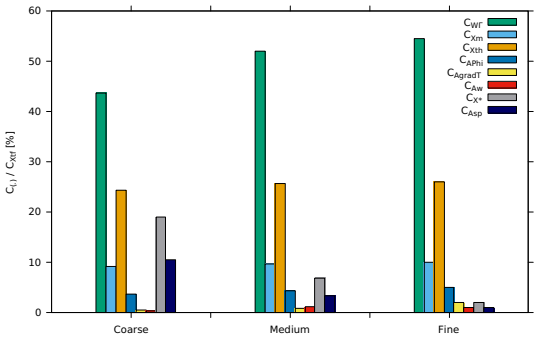

Figure 3: Grid convergence of the exergy balance using a body-force model of the fan-OGV at the ADP operating point, for $x_{tp}/D_{fan} = 1.0$.

Grid	$C_{W\dot{\Gamma}}$	$C_{\dot{E}_u}$	$C_{\dot{E}_{vw}}$	$C_{\dot{E}_p}$	$C_{\dot{\mathrm{X}}_{th}}$	$C_{\dot{\mathrm{A}}_\phi}$	$C_{\dot{\mathrm{A}}_{\nabla T}}$	$C_{\dot{\mathrm{A}}_w}$	$C_{\dot{\mathrm{X}}^*}$	$C_{\dot{E}^*}$	$C_{\dot{\mathrm{A}}^*}$	$C_{\dot{\mathrm{A}}_{sp}}$
C	0.436	0.082	0.011	-0.003	0.242	0.035	0.004	0.003	0.189	-0.015	0.174	0.104
M	0.519	0.086	0.012	-0.001	0.256	0.043	0.008	0.010	0.068	-0.006	0.062	0.033
F	0.544	0.087	0.012	-0.001	0.260	0.049	0.019	0.010	0.020	-0.002	0.018	0.009

Table 2: Grid convergence of the exergy balance for $x_{tp}/D_{fan} = 1.0$ (ADP/BF). Values are relative with respect to the $C_{\dot{\mathrm{X}}_{tf}}$ value at each grid level.

kinetic perturbation energy. Viscous and thermal anergy components increase with grid refinement, since velocity and temperature gradients are resolved by the grid at a greater accuracy. The shockwave anergy component is however shown to be in very good agreement between the medium and fine grid. The influence of grid density on the exergy balance results is expected due to the accuracy of this analysis relying on the resolution of flow features in the solution. An inadequate grid density and numerical dissipation of flow structures of interest (e.g. vortices, wakes and jets) leads to an unbalanced exergy equation at the discrete level. This exergy balance residual (cf. $C_{\dot{\mathrm{X}}^*}$ in the tabulated results) is significant on the coarse grid level, which is expected as it was generated mainly for preliminary numerical investigations and not intended for physical analyses. The reduction of $C_{\dot{\mathrm{A}}^*}$ in particular illustrates the improved grid resolution in the jet and wake with the finer grids, whereas $C_{\dot{\mathrm{A}}_{sp}}$ is shown to account for roughly half of the exergy balance residual in each case. It is finally noted that the $\dot{\mathrm{X}}_{tf}$ discrepancy with respect to the fine grid is roughly -1.1% for the coarse grid and -0.3% for the medium grid. Given the more reasonable size with respect to the finer one, the medium grid level is shown to give an overall reasonable accuracy, with the exception of the term $C_{W\dot{\Gamma}}$ (roughly 5% difference w.r.t. the fine grid). At least part of the above discrepancies in terms of grid convergence can be associated with the dissipative character of the min-mod limiter used in the convective flux discretization. It is however important to note that despite the fact that grid refinement is essential for the absolute values of the exergy balance components, trends of physical terms are well depicted, even on the coarse grid level.

Fig. 4 shows the resolution of flow structures downstream of the engine with mesh refinement. Results for the coarse grid (not shown), highlight the rapid numerical dissipation of the jet compared to the medium and finer grids. The medium grid however gives a similar flow structure to the fine grid, albeit not at the same peak anergy levels. This is to be expected because the wake refinement of the medium grid is not adequate to accurately resolve the flow field gradients in the jet region. The distortion of the anergy fields due to the angle of attack is also visible in the two finer grid levels.

Fig. 5 shows the evolution of irreversible exergy loss (i.e. anergy generation) by viscous effects and thermal diffusion as the downstream limit of the c.v. is extended.

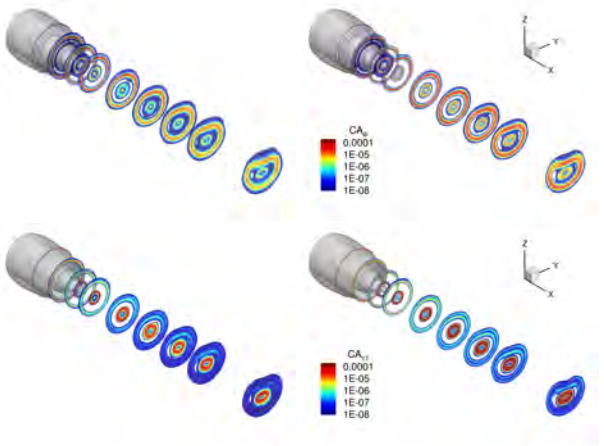

Figure 4: Viscous and thermal anergy generation at successive stations downstream of the engine (ADP/BF) for the medium (left) and fine (right) grids.

As discussed above, these terms rely respectively on the resolution of viscous stresses and thermal gradients present in the flow field, making grid quality and density essential to their precise computation. The inadequacy of the coarse grid in terms of resolution of the engine jet is clearly depicted, as viscous and thermal anergy evolutions remain almost stable beyond a distance of one fan diameter length downstream of the engine, indicating that the resolved gradients in the jet region are insignificant. However, they are better resolved by the medium and fine grids. The medium grid level seems able to capture part of the jet variations, although its solution is still not grid-converged. The fact that the fine-grid curve slope is not deteriorated suggests that the fine grid solution preserves a reasonable accuracy up to a few fan diameter lengths downstream of the engine. A difference can also be noted in the trend of the evolution of the viscous and thermal anergy terms, downstream of the nacelle. Viscous anergy increases significantly within the boundary layer in the near-wall regions (interior and exterior of the engine). A change of trend is then observed starting downstream of the secondary nozzle trailing edge, as viscous anergy is dominant in the mixing layer between the by-pass stream and the external flow (cf. also Fig. 4). On the other hand, thermal anergy is lower in the near-wall region and becomes dominant in the mixing layer between the primary and secondary stream jets. Its trend of increase is thus positioned slightly downstream of the nacelle trailing edge,

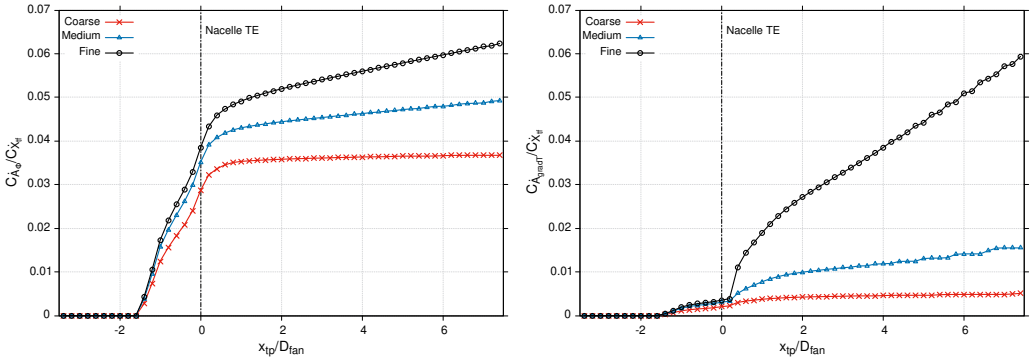

Figure 5: Evolution of viscous and thermal anergy by the variation of the c.v. downstream limit (ADP/BF).

	$C_{W\dot{\Gamma}}$	$C_{\dot{E}_u}$	$C_{\dot{E}_{vw}}$	$C_{\dot{E}_p}$	$C_{\dot{X}_{th}}$	$C_{\dot{A}_\phi}$	$C_{\dot{A}_{\nabla T}}$	$C_{\dot{A}_w}$	$C_{\dot{X}^*}$	$C_{\dot{E}^*}$	$C_{\dot{A}^*}$	$C_{\dot{A}_{sp}}$
AD-UP	0.525	0.087	0.011	-0.000	0.247	0.048	0.007	0.010	0.065	-0.006	0.059	0.031
AD-AB	0.525	0.086	0.011	-0.000	0.242	0.053	0.012	0.009	0.062	-0.006	0.057	0.031
BF	0.519	0.086	0.012	-0.001	0.256	0.043	0.008	0.010	0.068	-0.006	0.062	0.033

Table 3: Exergy balance for different fan/OGV models at $x_{tp}/D_{fan} = 1.0$ (ADP / Medium grid). Values are relative with respect to the $C_{\dot{X}_{tf}}$ value of each case.

at the exit of the primary stream. These results also show that within the downstream distance plotted in this figure, the part of viscous anergy generated in the near-wall region is larger than that generated within the mixing layers and the jet. The opposite stands for thermal anergy, which is dominant in the jet region.

In addition, sensitivity studies have been performed with respect to the upstream and lateral extension of the control volume of the exergy analysis, the numerical accuracy of the reconstruction of data on boundary surfaces, as well as some code parameters that are used to define physical integration volumes for exergy balance terms. These showed a satisfactory robustness of the exergy analysis results.

5.2 Fan/OGV model comparison

The current section presents a comparison between the actuator disk and body-force models discussed in Section 3 in terms of exergy balance, performed at the medium grid level. The BF computation corresponds to the medium grid of the previous section.

Relative values of the exergy balance coefficients are given in Table 3 and show very similar trends for all three models. An underestimation of the $C_{W\dot{\Gamma}}$ term can be however noted on the BF computation with respect to the two AD cases, the absolute values of which are in turn in closer agreement to the body-force computation on the fine grid. This is attributed to a slower grid convergence of the BF method with respect to the AD cases, an aspect which could be related to the dissipation of the min-mod limiter in the source term region. Furthermore, the BF computation shows lower viscous and thermal anergy generation. In particular, the thermal anergy of the AD-UP case is similar to the BF case, but its viscous anergy is increased. On the other hand, the AD-AB case shows an increase in both viscous and thermal anergy. Fig. 6 shows a comparison of the viscous anergy field in the engine interior for the three cases. This highlights a slight increase of viscous anergy generation near the actuator-disk conditions. In the AD-AB case however, two regions of flow separation can be identified at the OGV-hub and the OGV-shroud junctions, with the former generating higher levels of anergy between the two. On the other hand, viscous anergy levels in the body-force source term region are at lower levels compared to the AD cases. Last, it should be noted that the two AD computations have a higher rate of exergy inflow through propulsive surfaces ($C_{\dot{X}_{tf}}$) by 4-5% with respect to the BF case at the ADP operating condition. The numerical precision indicators are similar for the three computations.

5.3 Performance analysis at different operating conditions

This section presents a comparison of the exergy-based performance of the engine at different operating points. In particular, cruise performance (ADP point) is compared to low speed (LS) conditions at an angle of attack of 15° and 35° (henceforth referred to as LS15 and LS35 respectively). The latter corresponds to one of the off-design conditions investigated in the frame of the analysis of inlet distortion effects. The corresponding solutions were computed with the body-force approach on the medium grid level for all three operating points.

The overall exergy balance is presented in Fig. 7 and

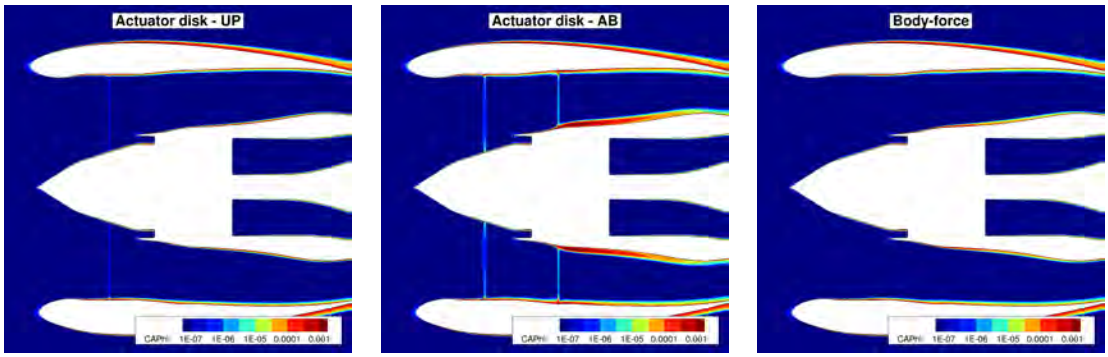

Figure 6: Viscous anergy close to the engine axis for the AD-UP, AD-AB and BF computations (ADP / Medium grid).

the corresponding coefficient values are given in Table 4. These results highlight that at the ADP operating condition a higher part of exergy inflow by the propulsive system is converted to thrust, corresponding to a higher overall exergetic engine efficiency. The portion of this exergy inflow that exits the control volume in the form of thermocompressible exergy ($C_{\dot{\mathrm{X}}_{th}}$) is in the same order of magnitude for all three cases. A significant change is however observed in terms of mechanical exergy outflow ($C_{\dot{\mathrm{X}}_{m}}$), which at low-speed is significantly higher than at the ADP conditions. It is interesting to note that the increase of this component is of the order of magnitude of the decrease of exergy consumption associated with thrust production, the sum of $C_{\dot{\mathrm{X}}_{m}}$ and C_{WT}, corresponding to 61-67% of the $C_{\dot{\mathrm{X}}_{tf}}$ component (i.e. the overall exergy inflow into the system through the fan/OGV source terms and the primary stream boundary conditions). The detailed exergy balance also highlights the decomposition of this mechanical exergy outflow into its streamwise and transversal components, the latter being increased at a higher angle of attack. Fig. 8 shows a visualization of exergy fluxes and the viscous and thermal anergy fields at a station downstream of the OGV. This figure clearly depicts that the inlet distortion due to the higher angle of attack of the LS35 case corresponds to a reduction of streamwise kinetic energy perturbation and a significant increase of the corresponding transversal component that persist downstream of the OGV. The $C_{\dot{\mathrm{X}}_{th}}$ field is also shown to be of generally lower magnitude at the LS35 point, but this conclusion is dependent on the survey plane position, as will be shown in the following. While anergy is limited to the near-wall region at the ADP condition, the same figure shows that the region of anergy production is enlarged in LS conditions due to the appearance of a flow separation at the inlet lip, which is then displaced due to the rotation introduced by the fan. This effect, clearly depicted in the field of local anergy production, is further discussed in the following.

Fig. 9 shows the variation of exergy outflow and anergy generation terms with the variation of the downstream limit of the control volume. This highlights the down-

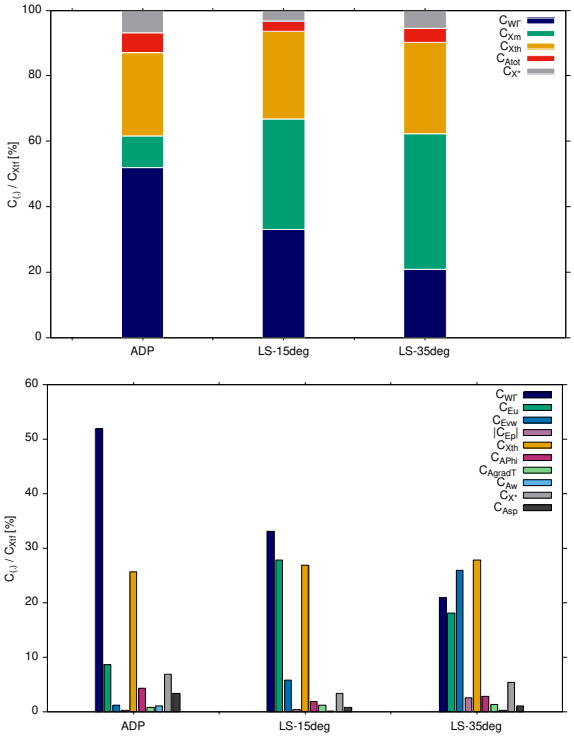

Figure 7: Exergy balance at different operating points of the engine (BF / Medium grid), for $x_{tp}/D_{fan} = 1.0$.

stream evolution of the exergy balance and the exchanges between different components, such as the transformation of reversible mechanical/exergy outflows to anergy generation through irreversible phenomena. Variations in the engine interior arise from the presence of the nacelle, spinner, fan, splitter, OGV, primary/secondary nozzle and plug, followed by the jet. As expected, the performance at the ADP is better than at the two LS conditions, which is visible in terms of lower mechanical/thermocompressible exergy outflows (i.e. reduced deposition, or waste, of exergy which will eventually be transformed into anergy by viscous effects in the jet/wake) and anergy generation terms (i.e. irreversible losses of exergy in the c.v.). An exception is the evolution of $C_{\dot{\mathrm{X}}_{th}}$, as the LS cases show

	$C_{W\dot{\Gamma}}$	$C_{\dot{E}_u}$	$C_{\dot{E}_{vw}}$	$C_{\dot{E}_p}$	$C_{\dot{\mathrm{X}}_{th}}$	$C_{\dot{\mathrm{A}}_\phi}$	$C_{\dot{\mathrm{A}}_{\nabla T}}$	$C_{\dot{\mathrm{A}}_w}$	$C_{\dot{\mathrm{X}}^*}$	$C_{\dot{E}^*}$	$C_{\dot{\mathrm{A}}^*}$	$C_{\dot{\mathrm{A}}_{sp}}$
ADP	0.519	0.086	0.012	-0.001	0.256	0.043	0.008	0.010	0.068	-0.006	0.062	0.033
LS15	0.330	0.277	0.057	0.003	0.269	0.018	0.012	0.001	0.033	-0.005	0.028	0.007
LS35	0.209	0.180	0.259	-0.025	0.278	0.028	0.013	0.002	0.054	-0.010	0.044	0.011

Table 4: Exergy balance components at different operating points for $x_{tp}/D_{fan} = 1.0$ (BF / Medium grid). Values are relative with respect to the $C_{\dot{\mathrm{X}}_{tf}}$ value of each case.

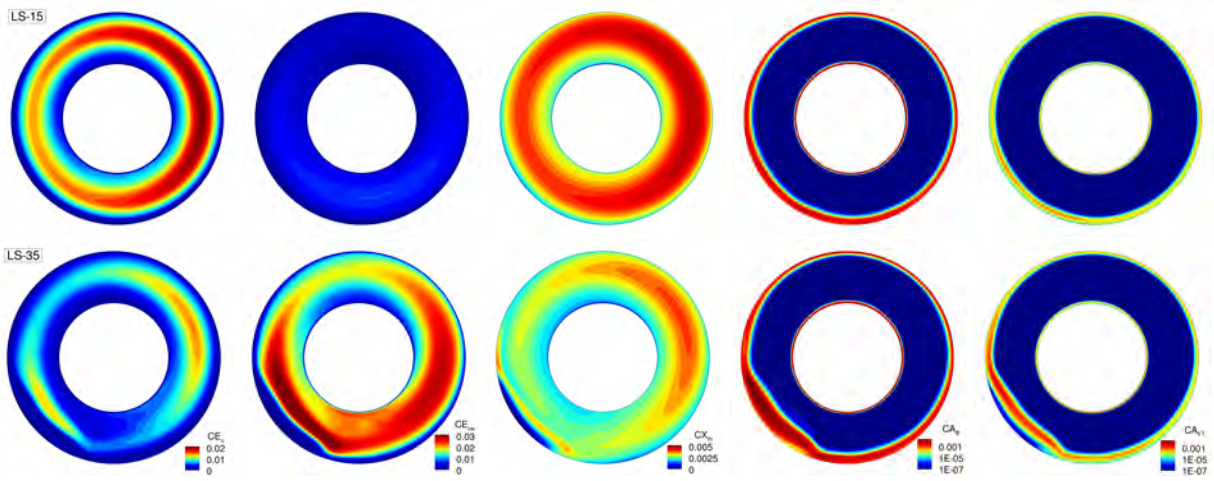

Figure 8: Exergy fluxes and anergy generation downstream of the OGV for the low-speed operating point at two different angles of attack (BF / Medium grid).

a steeper decline of this component moving away from the engine. All three cases feature a shockwave, whose trace is also present in the $C_{\dot{\mathrm{X}}_{th}}$ component and the corresponding losses are shown by the $C_{\dot{\mathrm{A}}_w}$ term in Table 4. At the ADP conditions, an annular shockwave is present in the nacelle exterior close to the fan/OGV position along the axis, in addition to a more localised shockwave positioned slightly upstream on the sides of the nacelle. At the LS conditions on the other hand, a shockwave is present at the lower internal side of the inlet lip and upstream of the fan position. The deflection of the jet at the higher angle of attack between the LS cases is visible both in the more significant reduction of streamwise kinetic exergy outflow and the respective increase of transversal kinetic exergy outflow, as well as that of thermocompressible exergy outflow after a distance of approximately 2 fan diameter lengths downstream of the nacelle trailing edge. Last, higher anergy generation is noted in the LS35 case due to the increased velocity and temperature gradients in the deflected jet. In the case of viscous anergy this is already notable in the near-wall region, likely due to the appearance of the flow separation in the lower side of the engine inlet. For thermal anergy the most significant increase at a higher angle of attack appears a bit further downstream, as already discussed in Section 5.1. It is also interesting to note that at LS conditions the main part of anergy generation takes place in the jet for both viscous and thermal anergy. Concerning viscous anergy, this is opposite to what is observed at ADP conditions where viscous anergy produced in the near-wall region is larger to that produced downstream of the engine.

A visualization of the viscous and thermal anergy fields for the three operating points is shown in Fig. 10. At LS conditions, anergy generation is notable on the inlet lip and is propagated downstream. Furthermore, at the LS35 operating point, a flow separation occurs on the upper part of the nacelle exterior surface, leading to the formation of a counter-rotating vortex pair (visible in Fig. 11). This in turn leads to an increase of exergy losses (i.e. anergy generation), which is more significant in terms of viscous anergy than in terms of its thermal counterpart. As discussed in previous sections, it is again shown that viscous anergy is dominant in the boundary layers and the secondary stream jet/free-stream mixing layer, whereas thermal anergy is dominant in the mixing layer between the primary and secondary stream jets. Finally, aside from the visualization of the vortex pair in the upper surface of the nacelle, Fig. 11 illustrates the mixing of the external flow with the engine jet downstream of the engine.

6. CONCLUSIVE REMARKS

The present work has consisted in the analysis of an isolated research UHBR engine using an exergy balance method. Grid convergence investigations have first been carried out at the aerodynamic design point of the engine, showing that exergy balance trends are well depicted on

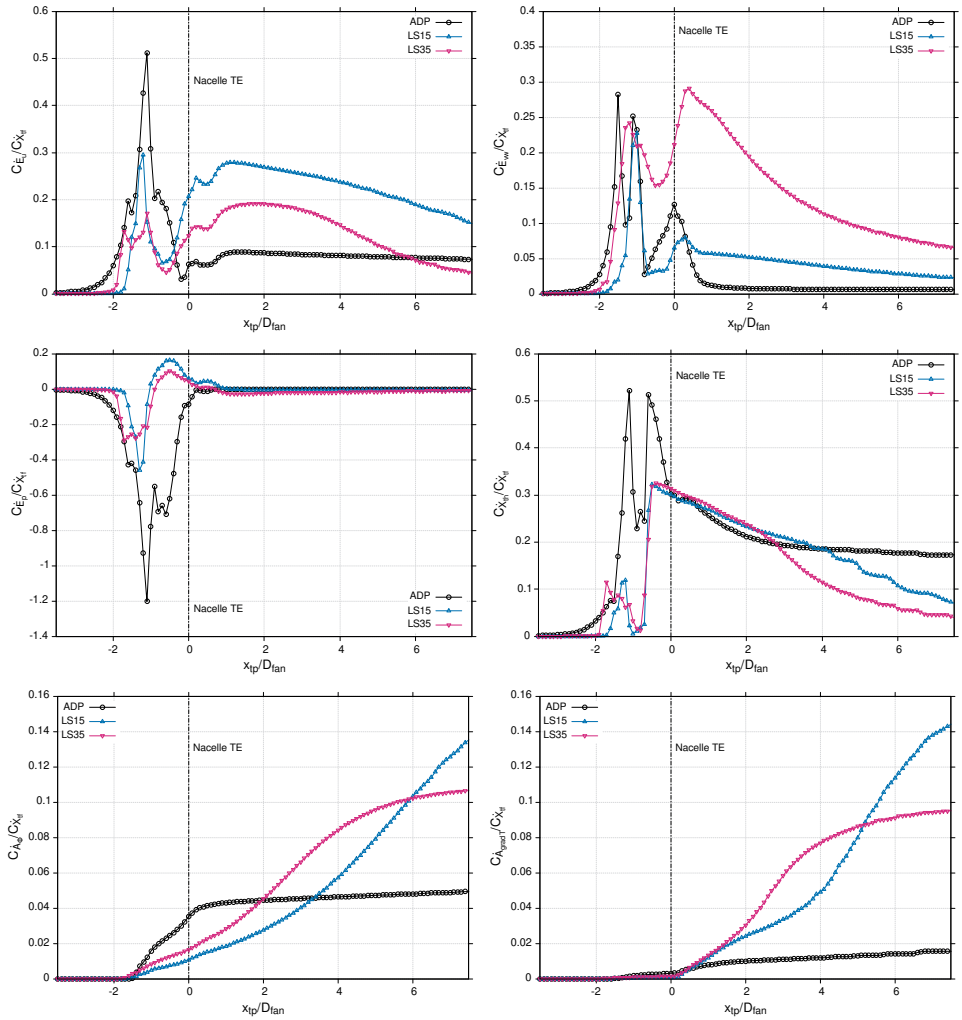

Figure 9: Variation of exergy balance components by the variation of the c.v. downstream limit at different operating points (BF / Medium grid).

coarser grids but an adequate grid refinement is required for accurate values of specific components. A comparative study has then been carried out in terms of methodology, in particular considering different simplified models for the fan and OGV that are common in design studies. This study has identified small differences (e.g. flow separation in one of the actuator disk cases) and provided a quantification of their influence, but shown an overall good agreement of the three models in terms of the exergy balance. Finally, physical analyses have been carried out at three different operating points, allowing to evaluate the engine performance and characterize the sources of efficiency loss in a non-nominal regime. The results obtained show that the exergy balance method can quantify the influence of complex flow phenomena occurring at different operating points on the engine performance, as well as localize flow regions where significant exergy losses take place. The latter is essential for the identification of areas with a margin for performance improvement in a design cycle. In terms of perspectives, the next step would be the analysis of higher-fidelity computations resolving the fan and OGV blades. Unsteady simulations require further developments of the existing exergy balance formulation, but steady computations in a rotating frame of reference can be analysed using the recently-developed adaptation for this purpose [5]. A recent decomposition, derived from a more physical point of view, may also yield a refined insight on the exergy balance components [6]. Finally, future studies will consider the analysis of effects of the engine installation on an aircraft configuration using the exergy balance.

ACKNOWLEDGEMENTS

The present research was carried out in the frame of the Clean Sky 2 Joint Undertaking under the European Union's Horizon 2020 research and innovation programme. The design and CFD computations of the research UHBR engine were carried out in the frame of the ASPIRE project (Grant agreement No 681856-2). The exergy-based performance analysis presented in this pa-

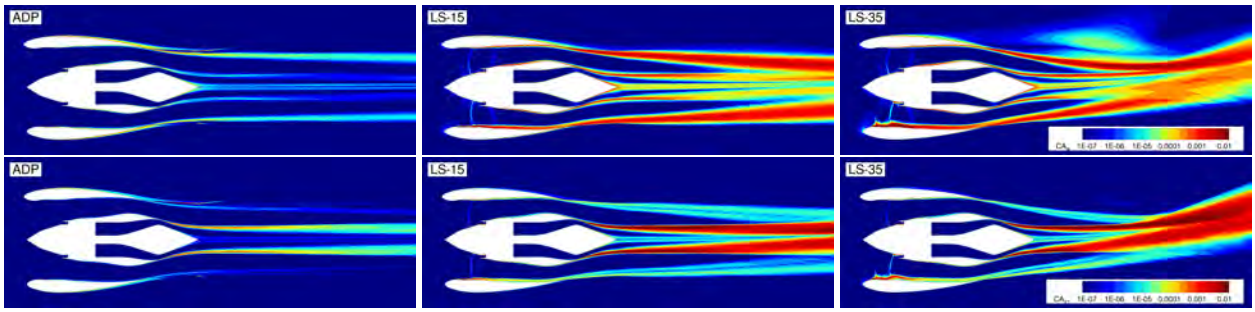

Figure 10: Viscous anergy (top) and thermal anergy (bottom) fields at different operating points (BF / Medium grid).

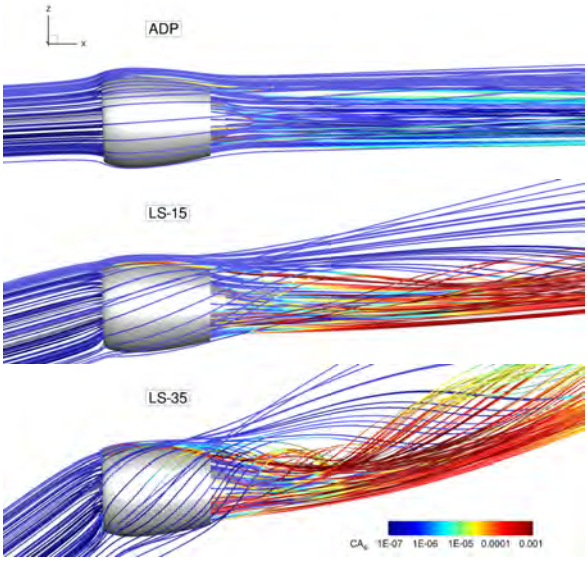

Figure 11: Streamribbons coloured by viscous anergy generation for the three different operating points of the ASPIRE engine (BF / Medium grid).

per was mainly carried out in 2020, within the ADEC project (Grant agreement No 945583). The studies presented have used the elsA software, whose development is partially funded by its three co-owners: ONERA, Airbus, and Safran. The development of the FFX software itself was supported by the French Directorate General for Civil Aviation (DGAC) in the frame of the NECTAR, SUBLIME and IDEFFIX conventions. The authors would also like to thank their colleagues A. Burlot and M. Vergez who contributed to the CFD computations of the ASPIRE engine, as well as those who worked in its design.

REFERENCES

[1] A. Arntz. *Civil Aircraft Aero-thermo-propulsive Performance Assessment by an Exergy Analysis of High-fidelity CFD-RANS Flow Solutions*. PhD thesis, Lille 1 Université - Sciences et Technologies, Lille, France, 2014.

[2] A. Arntz, O. Atinault, and A. Merlen. Exergy-based formulation for aircraft aeropropulsive performance assessment: Theoretical development. *AIAA Journal*, 53(6):1627–1639, 2015.

[3] D. Bailly, I. Petropoulos, C. Wervaecke, M. Méheut, O. Atinault, and C. Fournis. An overview of ONERA research activities related to drag analysis and breakdown. In *AIAA Aviation Forum, Paper 2021-2551*, 2021.

[4] C. Benoit, S. Péron, and S. Landier. Cassiopee: a CFD pre-and post-processing tool. *Aerospace Science and Technology*, 45:272–283, 2015.

[5] I. Berhouni, D. Bailly, and I. Petropoulos. Exergy balance extension to rotating reference frames: Application to a propeller configuration. *AIAA Journal*, 2023. Articles in advance, https://doi.org/10.2514/1.J062216.

[6] I. Berhouni, D. Bailly, and I. Petropoulos. On the adaptation of the exergy definition in the field of aerodynamics. In *57th 3AF International Conference on Applied Aerodynamics, Bordeaux, France*, 29-31 March, 2023.

[7] A. Burlot, F. Sartor, M. Vergez, M. Méheut, and R. Barrier. Method comparison for fan performance in short intake nacelle. In *AIAA Aviation Forum, Paper 2018-2926*, 2018.

[8] L. Cambier, S. Heib, and S. Plot. The Onera elsA CFD software: input from research and feedback from industry. *Mechanics & Industry*, 14(3):159–174, 2013.

[9] D. K. Hall. *Analysis of Civil Aircraft Propulsors with Boundary Layer Ingestion*. PhD thesis, Massachusetts Institute of Technology, 2015.

[10] M. Méheut, F. Sartor, M. Vergez, M. Laban, R. Schnell, A. W. Stuermer, and G. Lefevre. Assessment of fan/airframe aerodynamic performance using 360° uRANS computations: Code-to-Code comparison between ONERA, DLR, NLR and Airbus. In *AIAA Scitech 2019 Forum, Paper 2019-0582*, 2019.

[11] A. Peters, Z. S. Spakovszky, W. K. Lord, and B. Rose. Ultrashort Nacelles for Low Fan Pressure Ratio Propulsors. *Journal of Turbomachinery*, 137(2), 02 2015. 021001.

[12] I. Petropoulos, C. Wervaecke, D. Bailly, and T. Derweduwen. Numerical investigations of the exergy balance method for aerodynamic performance evaluation. In *AIAA Aviation Forum, Paper 2019-2926*, 2019.

[13] F. Sartor, A. Burlot, and M. Méheut. Numerical simulations of fan/airframe interaction with and without active flow-control. In *AIAA Aviation Forum, Paper 2018-3065*, 2018.